LUND UNIVERSITY
Faculty of Science

Influence of Ion-Ion Interactions on Single Qubit State Transfer Fidelities

Sofia Borgå

Thesis submitted for the degree of Bachelor of Science
Project duration: 2 months

Supervised by Prof. Stefan Kröll

Department of Physics
Division of Atomic Physics
June 2015

Abstract

Experimental single qubit gate fidelities in the rare-earth quantum computing (REQC) scheme was found to be lower than predicted by simulation of the optical Bloch equations for the system. The cause was believed to be excitation-induced frequency shifts (EFS), so this BSc thesis investigates a model for EFS in Eu:YSO where stochastic frequency shifts are imposed on the ions. This was implemented as a convolution of the solution to the Bloch equations in each time step with a convolution kernel, where the width of the kernel was dependent on the change in excitation. The simulation was run for a 7 µs complex hyperbolic secant pulse, one of the pulses used in previous experiments. The result was decreased fidelity, but not enough to explain the experimental result. This indicates that EFS may not be the main cause of the experimental fidelity losses, but more thorough investigation is required to draw more certain conclusions.

Acknowledgements

Foremost, I would like to thank my supervisor Prof. Stefan Kröll for sharing your expertise and taking your time with me. The project proved challenging in many ways but also rewarding when things started to come together. Few students at my level get the opportunity to learn from such a knowledgeable scientist. Moreover, I would like to express my gratitude towards all of the quantum information group. Sharing your collected expertise in various fields has served me several important pointers and pieces of advice during this project. Sitting in on group meetings and listening to countless insightful discussions has been a great learning experience for me. You have provided me with insights into the work of a research group that, again, few other students at my level get so see and for which I am sincerely grateful.

I would also like to thank my family, corridor mates and fellow students for your continued understanding and support during the project, be it late night, early morning or phone calls three times an hour if necessary. Without you I would not have been able to finish. Especially my mother, Åse Borgå, has put a lot of time and effort into getting me back on track when things got out of hand, which ultimately taught me a lot about myself and for which I will be forever thankful.

List of Abbreviations

DFT	discrete Fourier transform
EFS	excitation-induced frequency shift
FFT	fast Fourier transform
FWHM	full width at half maximum
NMR	nuclear magnetic resonance
RE	rare-earth element
REQC	RE-doped-crystal-based quantum computing
RK4	4th order Runge-Kutta method
YSO	Y_2SiO_5 (yttrium silicate)

Contents

Chapter 1

Introduction

This chapter introduces the reader to the key concepts and motives for this work. A brief introduction to the theory of quantum computing and the preceding experiments carried out by the quantum information group in Lund is provided, while the in-depth discussion is postponed to chapter 2. Understanding the results of experiments such as those performed in Lund is the main motivation for the simulation that constitutes the body of this thesis. Finally, the goals and scope of the work is discussed in section 1.3.

1.1 Introduction to Quantum Computing

By analogy to the binary unit of classical information and computation, the *bit*, a similar unit for quantum information, the *qubit*, can be defined. The qubit is a two-level quantum mechanical system with eigenfunctions representing 0 and 1 respectively, but contrary to the classical bit the qubit has not only the possibility to be in a state 0 or 1, but can also be in a *superposition* thereof. Classical bits are always independent and need to be addressed individually. For instance, it is not possible to prepare two bits such that a manipulation addressing only one of them automatically affects both. This is possible for qubits however, due to *quantum entanglement* which can be thought of as a superposition of more than one qubit. The field of quantum information and quantum computing evolves around harnessing the information carrying power of exotic effects such as superposition and entanglement.

Just like classical computation is represented by circuits of binary logical gates, also quantum computing can be represented using a model of circuits of *quantum gates*. There is an infinite number of potential quantum operations that could be represented as a quantum gate. It can be shown however, that a set of only four *universal* gate types is needed to perform any quantum operation with arbitrary accuracy. More complicated algorithms for carrying out some computation can then be constructed as circuits of such gates. Although quantum algorithms seem capable to perform many of the tasks of classical algorithms, quantum algorithms have to have some significant advantage over a classical counterpart to be of any real interest. Generally, there are three classes of algorithms with this characteristic [1, p. 37]. These are Fourier transform-based, quantum search and quantum simulation algorithms, and they all rely on the information compressing advantages of superposition and entangled states.

As the size of classical computer hardware approaches the limit where quantum effects can no longer be ignored, there will be the need for far better understanding and control of the quantum world than there is today. But for quantum computing to extend beyond

being a merely a theoretical curiosity, there has to be a way to physically implement qubits such that advantageous algorithms can be demonstrated. A working quantum computer would bring computational power enough to break the public key cryptographic systems on which much of today's information security relies. Also, the possibility to simulate larger scale quantum systems would have a tremendous impact on the natural sciences.

1.2 Preceding experiments in Rare-Earth Quantum Computing

Various implementations of qubits have been proposed and tested experimentally, and they all have their merits and drawbacks. The qubit system investigated in Lund uses hyperfine levels of the ground state of rare-earth (RE) dopant ions in inorganic crystals. Several combinations of dopants and host crystals have been investigated, although this thesis mainly concern europium-doped yttrium silicate, Eu^{3+}:Y_2SiO_5 or Eu:YSO for short. One of the merits of this system is the long life and coherence time of the hyperfine levels, which is mainly due to outer electron shells shielding the ground state from the atom's surrounding, allowing the state of the qubit to evolve undisturbed for relatively long periods of time.

Also, the resonance lines of the dopant ion species are strongly broadened by the crystal, where this band is made up of narrower lines corresponding to ensembles of ions in the crystal that happen to resonate at some frequency within the band. These ensembles can be addressed separately by tuning the frequency of the narrow-band laser light sent into the crystal. Therefore, RE doped crystals are said to be highly *frequency selective*. The frequency selective feature in combination with a technique called *hole burning*, where spectral regions are be emptied of absorbing ions by optical pumping them to other levels, allows ensembles of ions to be transferred between states by tailored laser pulses and series of pulses. This interaction between ion and light is described by the optical Bloch equations introduced in section 2.2.2.

Such an ensemble represents a qubit in the RE-doped-crystal-based quantum computing (REQC) scheme, thus known as an *ensemble qubit*. However, this approach poses a difficulty as the ensemble has to remain in the same state over time. The accuracy with which an ensemble can be transferred to a given state is known as *fidelity*, and loss of fidelity in the transfer to an intended state means losing the information that state represents. A previous simulation of single ensemble qubit state transfers, upon which this work is based, predicts the fidelity to be higher than 99.9% for a full population inversion. Experiments on the other hand have fidelities around 96-98% which is believed to be due to *excitation-induced frequency shifts* (EFS) of the resonance frequency of the ions. This shift occurs because the excitation of one ion changes the permanent electric dipole moment of that ion and thus the local electric field, imposing a Stark effect perturbing the neighbouring ions' levels. The effect on the obtained population in the excited state $|e\rangle$ is illustrated in figure 1.1 where a pulse of sweeping frequency ν has excited ions of all ensembles I through III in ascending order, thus inducing EFS to the degree where some ions are no longer in resonance and therefore left in their ground state $|g\rangle$.

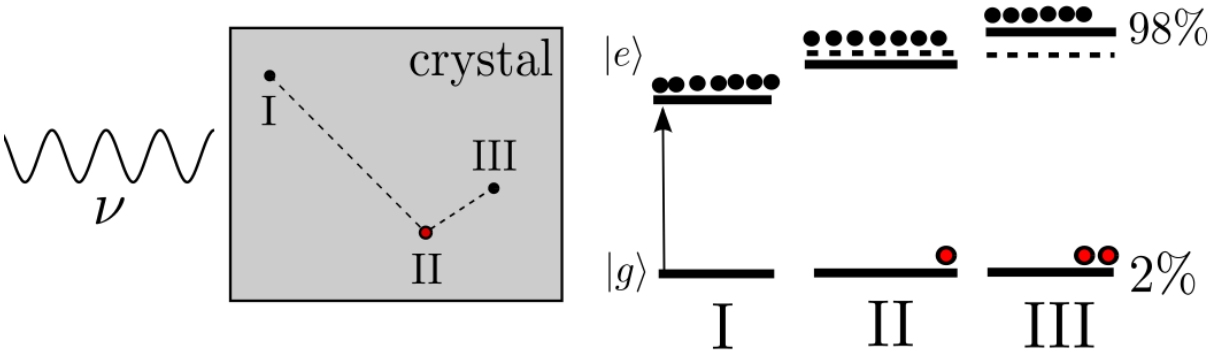

Figure 1.1 The pulse ν sweeps from lower to higher frequency. As ensemble I is excited, a small shift is induced for some ions of ensemble II. Most ions of ensemble II are can still be excited however. Moreover this induces a stronger shift on some ions of ensemble III, shifting them out of resonance with the pulse. The result is fidelity below 100%, or that full excited state population is not obtained. Note that this figure merely illustrate an example of how EFS can occur and is not intended to give the full picture. In reality, ions of all ensembles will be distributed randomly, and without preference to ions of similar resonance frequency as might be tempting to conclude from the figure.

1.3 Scope of the Thesis

The goal for this work, as set out at the beginning of the diploma work course, was to incorporate EFS due to dipole-dipole interaction into an existing simulation of the optical Bloch equations (2.4), introduced in chapter 2, for a single RE qubit in order to investigate whether dipole-dipole interaction could be the cause of the reduced qubit fidelity as found by experiment compared to the fidelity of the simulated qubit. How to model the interaction was not decided at that time, so naturally considerable time was spent trying to understand and adapt the chosen model to the physical system at hand.

Necessary background information is covered in chapter 2. The original MATLAB simulation and the incorporation of EFS effects is introduced in chapter 3. The model of EFS used is the sudden-jump model as described by Graf [2] but for a single laser pulse, and the implementation in MATLAB follows the example of Burr *et al.* [3].

Chapter 2

Background

The first part concerns quantum information and quantum computing at a general level. Section 2.1.1 introduces the qubit and other fundamental concepts in quantum information and quantum computing. The following sections 2.1.2 through 2.1.4 are intended to give a brief overview of how a quantum computer could operate, and some common examples of physical realisations are given in section 2.1.5. The second part provides the experimental background in the group's experiments. The physical system and methods for manipulating it are briefly introduced in sections 2.2.1 and 2.2.3. Section 2.2.2 discuss the Bloch equations in some detail as they provide the main tool for understanding the two-level quantum systems considered.

2.1 Quantum Computing

2.1.1 The Qubit

The fundamental unit of classical information – the bit – is the computational basis for all classical computation. It is a binary unit having either the value 0 or 1 and is easily represented physically, for example on the hard drive of a modern computer or the mechanical switches of the earliest realisations of a computing machine. By analogy, a similar fundamental information unit known as a *qubit* can be defined for quantum information. Qubits differ fundamentally from classical bits due to curious properties stemming from their representation in a two-level quantum mechanical system. In a system with two basis states, where the eigenfunctions represent 0 and 1 respectively, the system can by the superposition principle of quantum mechanics take on a state $|\psi\rangle$ that is any linear combination of the two basis functions,

$$|\psi\rangle = \alpha\,|0\rangle + \beta\,|1\rangle\,. \tag{2.1}$$

The complex amplitudes α and β represent the probabilities of finding the system in either of the respective states upon measuring, and can be arbitrary as long as they satisfy the normalisation condition $|\alpha|^2 + |\beta|^2 = 1$. The quantum states in equation 2.1 are given in Dirac notation, which will be used throughout this text. Using this probabilistic fundamental unit of information to perform computing tasks may seem cumbersome at first glance, but the application of basic principles of quantum mechanics opens new possibilities for carrying out computations. Notable examples of such applications are given in section 2.1.3.

The superposition property of a single qubit described above is one of the fundamental resources of quantum information, meaning that the creation and manipulation of states with the property can be thought of as 'fuelling' quantum information processing. Another crucial resource of quantum information is *entanglement*, which can be thought of as an inseparable superposition of two or more qubits. For example,

$$|\Psi\rangle = \frac{|00\rangle + |11\rangle}{\sqrt{2}}, \tag{2.2}$$

where $|ij\rangle$ represents the combined two-qubit system. This feature of quantum mechanical systems have historically been the subject of much debate as its interpretation contradicts our intuitive understanding of the physical world. Even if the qubits of the entangled pair are separated by a very large distance, a measurement on either qubit will automatically collapse the other qubit into the same state. Thus the shared state of the pair must be a non-local property.

2.1.2 Quantum Gates

Classical computation can be described using a circuit model, which turns out to be equivalent to the important Turing model, where the latter will not be further discussed in this text. Please refer to for example [1] or other standard textbook in quantum computing or classical computer science. The circuit model describes how binary bitwise operations constitute algorithms for performing some computational task. These bitwise operations are represented as *logical gates*, named after what logical operation they perform on the input bits. An analogous circuit model using *quantum gates* is the standard model for describing quantum computation, and is easily represented graphically. Figure 2.1 show examples of symbols representing classical and quantum gates respectively.

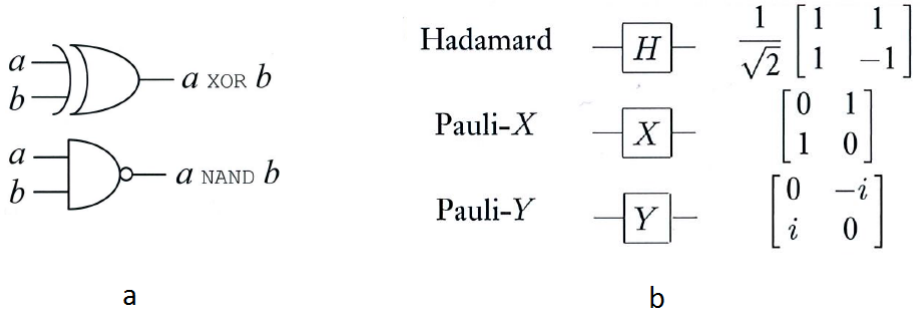

Figure 2.1 Examples of **(a)** classical logical gates operation on the bits a and b, and **(b)** single qubit quantum gates where the matrices are all unitary and represent transformations of the qubit. The Hadamard gate takes a state $|0\rangle$ or $|1\rangle$ to an equal superposition thereof, and vice versa. The pictured Pauli gates perform rotations an angle π about the u and v axes of the Bloch sphere in figure 2.3 respectively. Based on figures from Nielsen and Chuang [1, pp. 131, 177].

Conveniently, it can be shown for both classical and quantum computation that there exist sets of gates that are *universal*, meaning they can be put together such that they perform any computable task with arbitrary accuracy. In the case of quantum gates, some tasks may require polynomially or even exponentially many gates. The universality however, only means that the computation is in principle possible using the universal set; the solution may not be *efficient*. The concept of efficiency of a solution to a computational

problem is further discussed in section 2.1.3. In classical computation, the NAND gate is universal, providing that fixed work bits and copying of bits are available. Quantum computation requires a bigger set of gates generally consisting of both single and multiple qubit gates.

2.1.3 Quantum Algorithms

As mentioned in chapter 1, the quantum computer has to show some significant advantage over its classical counterpart to be of any relevance. There are a few notable algorithms where a quantum computer could have such an advantage over a classical computer in terms of time complexity, or how the time needed to solve the problem scales with the size of the input. Common notation is $\mathcal{O}(x)$, where x is some function describing how the execution time of some algorithm scales the number of input bits or qubits n. If the function x is some exponential 2^n or higher order, the solution is said to be *inefficient*. Common for these *quantum algorithms* is that their inefficiency for solving certain problems classically is either a limiting factor, when simulating quantum systems for example, or an exploited characteristic, in the case of public key encryption. There are three classes of such algorithms [1, p. 37], algorithms based on the quantum Fourier transform, quantum search algorithms and simulation algorithms, where a quantum computer is utilised for simulation a quantum system.

2.1.4 The DiVincenzo Criteria for a Quantum Computer

There is a set of criteria for a quantum computing machine commonly referred to as the DiVincenzo criteria in honour of the author. These define what characteristics are required of a computing machine operating in the quantum regime. DiVincenzo stated [4] the following requirements:

1. *The qubits are well characterised and the physical system is scalable.*
2. *It is possible to prepare a known initial state of a computation.*
3. *The coherence time of the system is much longer than the gate operation time.*
4. *It is possible to construct the set of universal quantum gates.*
5. *It is possible to read out the result of the computation.*

These criteria state only a bare minimum of requirements. The requirements on a computing machine able to perform the algorithms discussed in section 2.1.3 will for example require a large number of qubits in addition to the above requirements. Criteria 2, 4 and 5 hardly require further discussion. However, criteria 1 and 3 are less obvious and deserve some explaining.

The first of the DiVincenzo criteria concerns how well the two-level system constituting the qubit is known. Generally, the internal Hamiltonian, any couplings to external fields or other states of the qubit as well as the interaction with other qubits have to be known with some accuracy. The system also has to be scalable to a certain extent in order to be of any practical use, meaning it is possible to create and operate on a qubit register of the size required for the task.

The third criterion concerns the *coherence* of the quantum system. All quantum systems considered until this point have been assumed to be infinitely coherent. In reality however, this is never the case as the outside world will interact with the system thus causing it to change into some for us unknown state, or *decohere*. This will inevitably also be the case for any qubit implementation. On the other hand, infinite coherence is not required as this criterion states; the lower bound on the time during which the system evolves in a predictable way is the time it takes to operate on the state with a quantum gate.

2.1.5 Physical Qubit Realisations

The following section summarises the content of chapter 7 in Nielsen and Chuang [1], and is intended to provide a brief overview of what types of schemes have been proposed and tested as possible systems for realising a quantum computer.

Coherent photons One obvious candidate for a coherent quantum system is the photon, which has in principle infinite coherence time even in the presence of other photons. Various schemes using either photon polarisation or cavity modes as qubits have been proposed. Quantum gates can be constructed from phase shifters, beamsplitters and some devise to mediate a photon-photon coupling, cavities containing a few atoms to which the light couples in the case of a cavity scheme. The photon-photon coupling poses difficulties to implement multi-qubit gates needed however required to fulfil the fifth DiVincenzo criterion.

Nuclear spin Nuclear spin qubits utilising nuclear magnetic resonance (NMR) techniques differs from the other schemes presented here, as the qubits consist of ensembles of around 10^{18} molecules. The molecules are placed in a strong magnetic field and then manipulated using magnetic field pulses. The coupling between qubits is provided by the chemical bonds within the molecules. However, the efficiency of the readout decreases exponentially with the number of qubits making scaling of the system very limited.

Trapped ions One of the most successful schemes so far uses hyperfine ground state of trapped ions at low temperature. By applying suitable laser pulses the state of single ions can be manipulated, and shared low phonon modes can be used for multi-qubit operations. However, the phonon coherence time is short which limits the scalability of the scheme, and cooling the ions down to their motional ground state is difficult.

Semiconductor-based schemes Maybe the more promising class of schemes for the future are schemes based on semiconductor materials. For example quantum dots, confined Cooper pairs in superconductors and magnetic flux through superconducting loops has been proposed as qubits. Although being limited by their short coherence time, these types of schemes have the great advantage of already existing infrastructure for semiconductor research and large scale manufacture, making them yet promising for the future.

2.2 Rare-Earth ion Quantum Computing

The quantum computing scheme discussed in the rest of this work is rare-earth metal dopant ion in a crystal, and is maybe closest related to the NMR scheme mentioned in section 2.1.5. The two-level system is two hyperfine ground state levels of rare-earth ions (RE) as in the case of trapped cold ions. But as the RE ions sit in a crystal, ensembles of ions are addressed using tailored laser pulses. Multi-qubit operations are mediated by ion-ion interactions, which are, however, believed to ultimately limit the coherence. Understanding the influence and nature of decoherence due to ion-ion interactions lie at the heart of this thesis.

2.2.1 Ensemble Qubits in RE Doped Crystals

Rare-earth ion doped crystals are attractive materials for quantum computer hardware for a number of reasons, mainly related to their coherence properties. First of all, Eu and other rare-earth metals have partly filled 4f shells which are shielded from the environment by 5s and 5p shells, spatially located outside the 4f shells. Long lifetimes T_1 and coherence times T_2 of states within the 4f shell are maybe largely due to being shielded by the 5s and 5p shells. Therefore, ground state hyperfine levels in the 4f shell pose a good two-level candidate for a qubit.

Ions of rare-earth elements can be used as a dopant in inorganic transparent crystals, like yttrium silicate Y_2SiO_5 where it can replace any of the two inequivalent yttrium sites. At cryogenic temperatures of a few K, there are few phonons and thus low probability of phonon interactions and there is no Doppler broadening as the ions are fixed in space. There are other broadening mechanisms however. The crystal lattice is not ideal as the dopant ions and other impurities distort the symmetry of the crystal and thus the local environment of the individual ions, which results in broadening of the dopant ions' spectral line. When discussing absorption and emission by ions in a crystal, there is the need to distinguish the *inhomogeneous* linewidth Γ_{inh} from the *homogeneous* Γ_h. The first is due to static interactions, such as inhomogeneities in the electric field within the crystal, and depend on the absorber species at hand. The second is due to relaxation and dynamical processes, and will be the same for all ions in the crystal [5, p. 9]. For our purposes, the inhomogeneous linewidth can be seen as the sum of the homogeneous linewidths, as shown by figure 2.2. An ensemble of ions in the crystal resonating at some frequency within the inhomogeneous linewidth constitutes a qubit, and thus the maximum number of qubits in the crystal is limited by the ratio Γ_{inh}/Γ_h as this is the number of distinguishable frequency channels addressable by the laser. Furthermore, it is also possible to filter out and address ensembles of ions within Γ_{inh} that are located spatially close to each other, and therefore interact strongly, to perform multi-qubit operations.

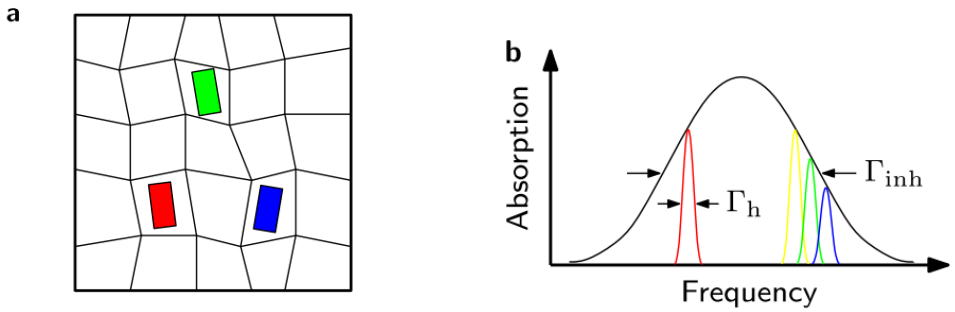

Figure 2.2 The relatively narrow homogeneous linewidth Γ_h, caused by relaxation and other dynamical processed, is the same for all ions. The inhomogeneous linewidth Γ_{inh} is due to distortions in the crystal lattice **(a)** and can be seen as the sum of the homogeneous linewidths **(b)**. Figure from [6].

2.2.2 The Optical Bloch Equations

In order to prepare and read out the state of a qubit, one needs to be able to predict the time evolution of the two-level system. From the time dependent Schrödinger equation for a two level quantum system in an electromagnetic field, a set of three coupled equations describing the evolution of the system can be derived. By taking into account that the upper state has a finite life time T_1, and that the system has a finite coherence time T_2 during, the optical Bloch equations (2.4) are obtained. The results of the derivation is summarised below, see for example Foot [7] for a detailed treatment.

For a coherent light pulse with electric field component $\mathbf{E}$, the *Rabi frequency* is given by

$$\Omega = \frac{\langle g| \, e\mathbf{r} \cdot \mathbf{E} \, |e\rangle}{\hbar} \tag{2.3}$$

for two levels[1] labelled g and e respectively and with $\mathbf{r}$ being the electron's distance from the atom's centre of mass, making $e\mathbf{r}$ the energy of the dipole. The Rabi frequency is in general complex so with Ω_{re} and Ω_{im} representing the real and complex parts respectively, the optical Bloch equations for the evolution of a two-level system read

$$\frac{\partial u}{\partial t} = -\frac{1}{T_2}u + \Delta v + \Omega_{im} w, \tag{2.4a}$$

$$\frac{\partial v}{\partial t} = \Delta u - \frac{1}{T_2}v + \Omega_{re} w, \tag{2.4b}$$

$$\frac{\partial w}{\partial t} = -\Omega_{im} u - \Omega_{re} v - \frac{1}{T_1}(\omega_0 + \omega). \tag{2.4c}$$

where ω_0 is the atomic resonance frequency and ω is the frequency of the light field. Here w is interpreted as the difference in population between the two levels, and u and v as how the population difference u of a superposition between the two levels will oscillate in time.

To illustrate the meaning of the Bloch equations, the Bloch vector is defined as

[1] These two levels will be between one of the qubit levels 0 or 1 and an intermediate excited state, not between 0 and 1 as 4f-4f dipole transitions are generally forbidden.

$$\mathbf{R} = u\hat{\mathbf{e}}_1 + v\hat{\mathbf{e}}_2 + w\hat{\mathbf{e}}_3, \tag{2.5}$$

which is a vector on the unit sphere, or *Bloch sphere*, since $|\mathbf{R}|^2 = |\mathbf{u}|^2 + |\mathbf{v}|^2 + |\mathbf{w}|^2 = 1$. The Bloch equations can then be restated as

$$\dot{\mathbf{R}} = \mathbf{\Omega_T} \times \mathbf{R} \tag{2.6}$$

where $\mathbf{\Omega_T}$ is analogous to a torque vector[6, p. 22] of the form

$$\mathbf{\Omega_T} = -\Omega_{re}\hat{\mathbf{e}}_1 + \Omega_{im}\hat{\mathbf{e}}_2 + \Delta\hat{\mathbf{e}}_3. \tag{2.7}$$

Thus the coherent evolution of a two-level system can be understood pictorially as the movement of the Bloch vector on the Bloch sphere. It is also straightforward to illustrate the concept of pulse area assuming the envelope of the pulse varies slowly[6, p. 24],

$$\Theta(t) = \int_0^t \Omega_{re}(t')dt', \tag{2.8}$$

in terms of the Bloch formalism. A pulse area of $\pi/2$ rotates the Bloch vector the same angle about the $\hat{\mathbf{e}}_1$ axis, and similar for $\Theta = \pi$ and $\Theta = 2\pi$ as shown in figure 2.3.

However, the trace of the Bloch vector over the surface of the Bloch vector for a particular pulse may not be in a plane as shown in figure 2.3. A commonly used pulse in the context of REQC is the complex hyperbolic secant pulse, or *sechyp* for short, where the Rabi frequency is given by

$$\Omega(t) = \Omega_0 \left\{\text{sech}\left[\beta(t - t_0)\right]\right\}^{1+i\mu} \tag{2.9}$$

for some Rabi frequency Ω_0 at the mid-time t_0, width parameter β and real constant μ. This pulse has a an effect on both ions on resonance with the light field and those slightly detuned while leaving ions resonating outside some frequency range unaffected, which is an advantage when performing operations on an inhomogeneously broadened system. The trace of the Bloch vector when a system interacts with a sechyp pulse will be a circulating trace as shown in figure 2.4, although slightly varying depending on the detuning.

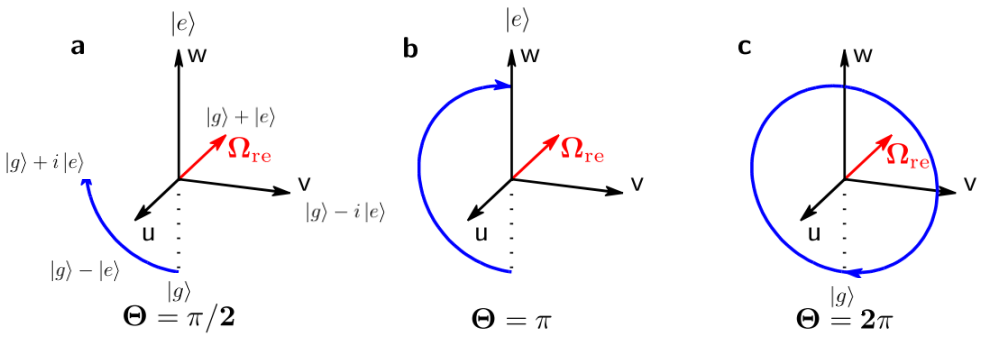

Figure 2.3 Rotation of the Bloch vector about the $\hat{\mathbf{e}}_1$ axis, starting from the ground state, for different values of the pulse area Θ. Figure from [6, p. 24].

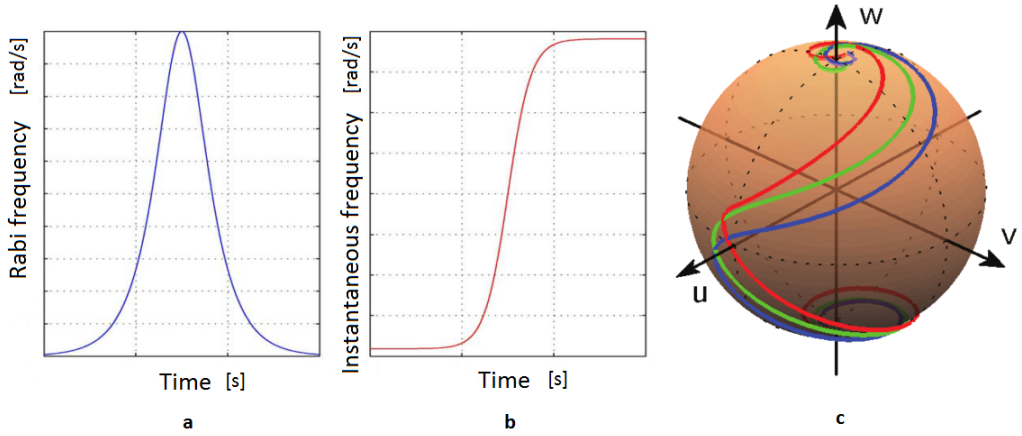

Figure 2.4 **(a)** Pulse envelope, **(b)** frequency sweep and **(c)** traces on the Bloch sphere for slightly different detunings Δ. Typically, the frequencies are of the order of MHz and the time of µs. Based on figures from [6, pp. 30-31].

2.2.3 Qubit Preparation Using Spectral Hole Burning

Eu:YSO, being a material with inhomogeneously broadened optical transitions, also exhibit a *hole burning* mechanism. Consider the hyperfine structure of the $^7F_0$ and $^5D_0$ levels shown in figure 2.5. The separations of the excited state levels are smaller than those between the ground state levels, so the excited state can be considered to be a single level for now. By tuning a laser to the resonance frequency of the level labelled $|0\rangle$, the absorbers in that levels are excited, after which they decay to either of the three ground states. By cycling the transition for some time the level can be emptied of absorbers which will all have gone to the other two levels, a method known as *optical pumping*. Now a laser is scanned in frequency over the spectral region of the $|0\rangle$ resonance frequency, where decreased absorption at the resonance frequency will create a *spectral hole* in the inhomogeneous absorption profile.

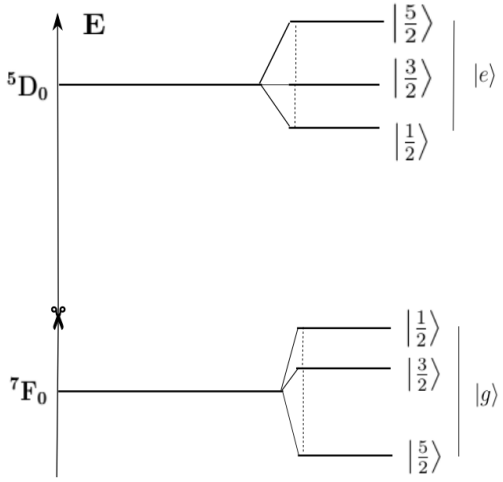

Figure 2.5 The level structure of Eu^{3+}.

However, the existence of several excited state levels will also cause *side holes* at distances from the centre hole corresponding to the excited level separations. Furthermore, the ground state separation, of the order of tens of MHz, is smaller than the inhomogeneous linewidth, of the order of GHz, so any absorbers decaying to the other ground states will result in increased absorption at their respective resonance frequencies. When scanned over, this mechanism will have created *anti-holes* at frequencies resonant with transitions between these levels and the excited state levels. The result from burning at a single frequency will thus be a complicated structure of holes and anti-holes.

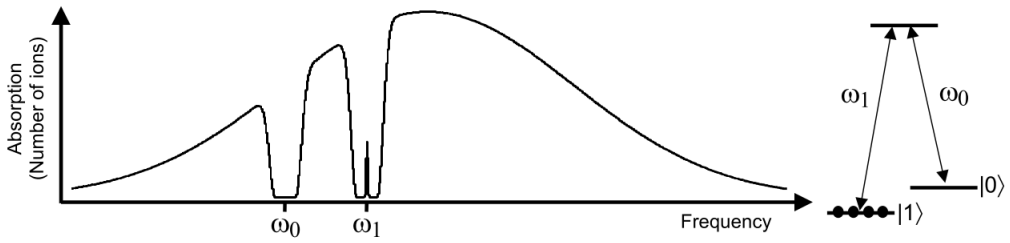

Figure 2.6 Two spectral pits, around ω_0 and ω_1 respectively, have been prepared within the inhomogeneous absorption line. An ensemble of ions that could represent a qubit has been prepared at ω_1. Figure from [5, p. 24].

By widening the frequency range of the burning pulse, a wider spectral region known as a *spectral pit* such as around ω_0 in figure 2.6 can be created. The pit is a region close to empty of absorbers, which will all have been pumped to levels resonant with frequencies outside the pit. The pumping to other ground state levels is also what limits the pit width. The hyperfine splitting of the states is the same for all homogeneous ensembles, and a single burning pulse can neither excite absorbers in the highest ground state level to any of the exited levels nor excite to the lowest excited state levels from any of the ground state levels. The width is thus limited by the difference between the ground and excited hyperfine splittings. By clearing the regions around the resonance frequencies of the $|0\rangle$ and $|1\rangle$ levels followed by limiting the burning to a narrower frequency range, some specific homogeneous ensemble can be transferred back into any of the two pits, or a superposition thereof, by the methods described in section 2.2.2. Thus an ensemble qubit has been prepared in a state such as around ω_1 in figure 2.6 that can be manipulated and read out.

2.2.4 Dipole-dipole Interaction Between RE Ions

There are several ways for ions in a crystal to interact, but only the type of interaction involving static electric dipole moments will be considered in this work. Ions with a difference in static electric dipole moment $\delta\mu$ between the ground and some excited state will influence its environment when it absorbs a photon. When the dipole field surrounding the ion changes due to the excitement of the ion, the energy levels of spatially neighbouring ions acquire a shift $\delta\nu$, known as an *excitation-induced frequency shift* (EFS), in resonance frequency as illustrated by in figure 2.7. This shift can be toward lower or higher frequency, and the magnitude of the shift should scale as $1/r^3$, where r is the separation, since this is how the strength of a dipole field scales. The result on an absorption peak as in figure 2.8 for example, is broadening, so the ions having their resonance frequency shifted will longer belong to the same homogeneous ensemble. The broadening effect is proportional to the density of excited ions. If the impact of EFS is strong, as for a high excitation density, a qubit cannot undergo many operations before the coherence of the ensemble, and thus the information, has been lost. Therefore, understanding of whether EFS is a major cause of lower-than-expected experimental fidelities is crucial for assessing the prospects of the REQC scheme.

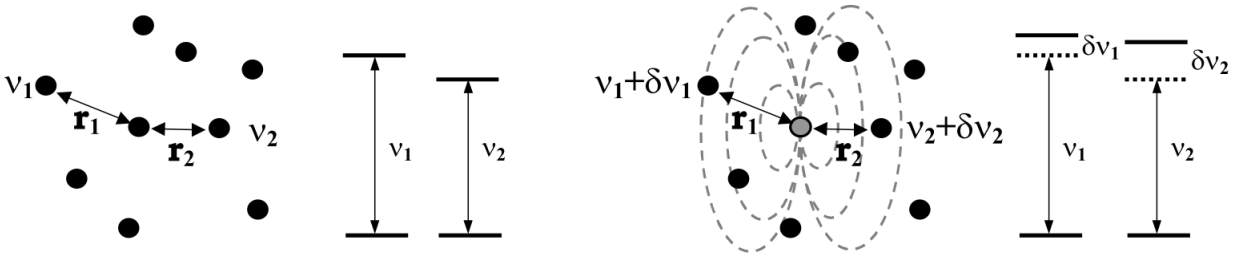

Figure 2.7 The excitation of the middle ion changes it's electric dipole moment, causing excitation-induced frequency shifts (EFS) $\delta\nu_i$ in it's neighbours. The magnitude of the shifts decrease with separation alike the strength of the dipole field, which decreases as $1/r^3$. Figure from [5, p. 15].

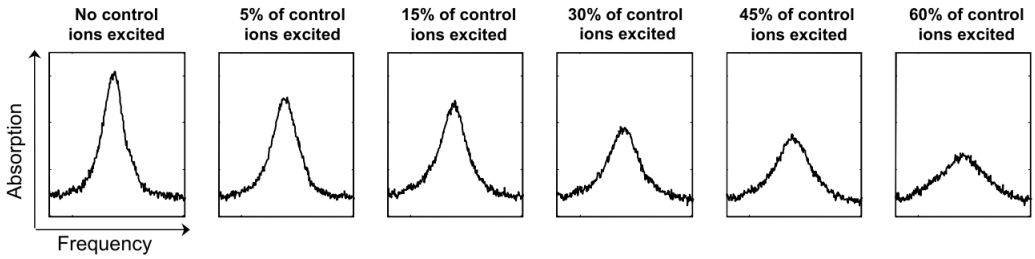

Figure 2.8 EFS cause broadening of spectral features, such as the absorption peak pictured here. The broadening is proportional to the density of excited ions. Figure from [5, p. 16].

Chapter 3

Implementation of Dipole-Dipole Interaction in the Bloch Simulation

This chapter presents a model for describing EFS and how this model is implemented in the MATLAB simulation constituting this thesis. To keep the discussion at the general level, definitions and algorithms are placed in appendices A and B. For the same reason, all program code is placed in appendix C, where it has been split up in sections corresponding to their function in the simulation for ease of reading.

The first part 3.1 describes in detail how the EFS can be modelled by assuming stochastic jumps in resonance frequency of each homogeneous ensemble of Eu ions, based on the overall excitation at each point in time. The last part 3.2 describes how the EFS model discussed in the previous section can be incorporated into the solving of the Bloch equations using convolution.

3.1 Stochastic frequency jump model of EFS

To simplify the modelling of EFS, dipole-dipole interaction between detuned ions only is considered in the following treatment. It has been shown analytically[8] that the probability distribution for obtaining a shift in resonance frequency due to a random distribution of dipoles has a Lorentzian shape,

$$L(\Delta) = \frac{1}{2\pi} \frac{\Gamma_{br}}{\Delta^2 + \Gamma_{br}^2/4}, \tag{3.1}$$

where Γ_{br} is the FWHM. As mentioned in section 2.2.4 the broadening by EFS is proportional to the density of excited ions in the crystal,

$$\Gamma_{br} = \Gamma_{efs} \langle w \rangle_{\Delta}, \tag{3.2}$$

where $\langle w \rangle_{\Delta}$ is the population difference w from the Bloch equations (2.4) averaged over detuning Δ and Γ_{efs} is the strength of the dipole-dipole interaction. The strength of the interaction can be derived from first principles [2, pp. 121-125], by assuming that the time-dependent resonance frequency of some ion is given by the sum of the intrinsic resonance frequency and the dipole-dipole interactions with ions at all other lattice sites in the crystal occupied by a dopant ion. The broadening Γ_{br} of each homogeneous ensemble at some time can be obtained from the macroscopic polarisation in the crystal, averaged

over site occupations, stochastic excitations of the ions, and relative angular distribution of the ions' dipole moments. The strength Γ_{efs}[1] is found to be[9]

$$\Gamma_{efs} = \frac{\pi}{3} p \langle|\kappa|\rangle D_0 \tag{3.3}$$

where p in equation (3.3) is the probability that a lattice site in the host crystal is replaced by a dopant ion, and $\langle|\kappa|\rangle$ is a geometrical factor due to the relative orientation of the dipoles, ranging from $4/\sqrt{27}$ when the dipoles are all parallel and $2/\pi$ when perpendicular with respect to the origin [10]. The dipole-dipole interaction D_0 at the lattice unit distance r_0 is given by

$$D_0 = \eta(0)\frac{(\delta\mu)^2}{4\pi\epsilon_0\hbar r_0^3} = \frac{h\zeta_S^2}{2\epsilon_0\epsilon(0)r_0^3} \tag{3.4}$$

for interaction ions with difference in permanent dipole moment $\delta\mu$ between ground and excited states. Here h and $\hbar$ are the Planck and reduced Planck constants respectively, ϵ_0 is the permittivity in vacuum and $\epsilon(0)$ is the dielectric constant of the crystal. As expected, the interaction scales as $1/r_0^3$. The last equality of equation (3.4) is a result of replacing $\delta\mu$ with the expression containing the Stark coefficient ζ_S in equation (7.27) of [2, p. 129], which also reduces the dielectric correction [11] $\eta(0)$ to $1/\epsilon(0)$.

In the context of incorporating EFS into the solving of the Bloch equations, the broadening effect of excitations at one point in time on the next is of interest. Therefore, the broadening Γ_{br} can reformulated as a width increment Γ_{br}^t between two discrete points in time[3],

$$\Gamma_{br}^t = \Gamma_{efs}\int_\Delta |w^t - w^{t-1}| g(\Delta) d\Delta. \tag{3.5}$$

where the integral returns the excitation density accumulated between time steps t and $t-1$, averaged over detuning and the inhomogeneous line profile $g(\Delta)$, which is another Lorentzian.

3.2 Simulating population transfer in the presence of EFS

The model of EFS described in section 3.1 requires the computed Bloch component w from both the current and the previous time steps in order to calculate the integrand of equation (3.5), and for all detuning steps in order to compute the integral. This prohibits the use of built-in MATLAB functions such as `ode45`, which returns the full solution to the input differential equation over the entire range of the variable. The only way to use such a function would be to incorporate the integral (3.5) into the Bloch equations (2.4) but, since the integrand contains the difference in the Bloch component w between two consecutive time steps, this is not so easily done. Therefore, the Bloch equations are solved using a standard fourth order Runge-Kutta method (RK4), as described in appendix A, thus allowing the width of the Lorentzian Γ_{br}^t to be calculated in each time step during the solving of the Bloch equations.

[1]Note that the notation here differs slightly from that in Graf [2]. The Γ_{br} stated here is equivalent to the Γ_{EFS-D} given in Graf. Here Γ_{efs} corresponds to the factor $\frac{CD_0}{2\pi}$ in Yan [9].

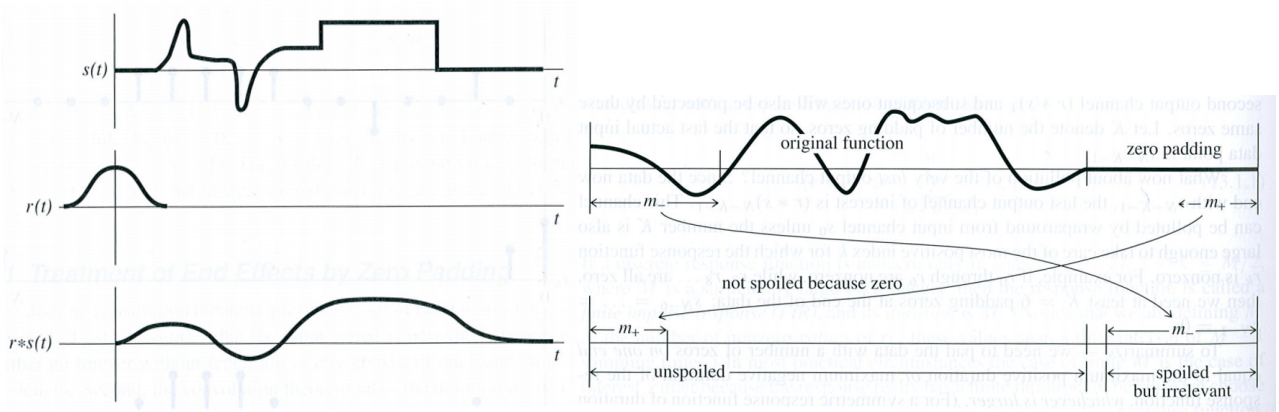

(a) **(b)**

Figure 3.1 **(a)** The smoother $r * s(t)$ is the convolution of some function $s(t)$ with the kernel $r(t)$. Figure from [12, p. 641]. **(b)** Extending the sequence to be convolved with zeros that are discarded after the convolution prevents leakage of the kernel into the convolved sequence. Figure from [12, p. 644].

The effect of EFS on spectral features, such as the absorption peak in figure 2.8, is broadening and flattening. By convolving the solutions to the Bloch equations in a given time step with the probability distribution $L(\Delta)$ for obtaining some shift in resonance frequency Δ, the Bloch components u, v and w are smoothed in accordance[2]. The principle is shown in figure 3.1a, where a some function $s(t)$ is convolved with a kernel $r(t)$ and the result is the convolution $r * s(t)$ which has smoother and broader features than $s(t)$. Furthermore, in order not to distort the scale of the Bloch components, the probability distribution $L(\Delta)$ has to be appropriately normalised. In a computer simulation, the detuning range is always discrete and finite, why $L(\Delta)$ has to sum to 1 over the detuning range. This is achieved by dividing each element of the discrete sequence by the sum of the sequence.

A fast way to compute a discrete convolution is using discrete Fourier transforms (DFT), in particular the Fast Fourier Transform (FFT) algorithm which is implemented in the `fft` function in MATLAB. The discrete convolution and the DFT are defined in appendix B. The inverse convolution theorem states that the convolution of two functions is equivalent to the inverse Fourier transform of the product of the respective forward transforms. However, the theorem puts constraints on the functions we wish to convolve. First, the sequences have to be of the same length, and second, the kernel is presumed to be a periodic function [12, p. 643]. The kernel used for this simulation has a profile much narrower than detuning range that is being simulated, but equal length of the respective sequences is easily achieved by defining the kernel $L(\Delta)$ over the entire detuning range of the Bloch components. Neglecting the second constraint would have the kernel 'leaking' into the end-points of the convolved signal as a consequence. Therefore, one end of the functions to be convolved can be padded with a number of zeros equal to the half the

[2]Since EFS also has a smoothing effect on the inhomogeneous spectral line $g(\Delta)$ which is used to compute the integral 3.5, $g(\Delta)$ too has to be convolved with $L(\Delta)$. This is precisely the case shown in figure 2.8. However, in the present case this effect is very small.

non-zero extent of the kernel. To maintain equal lengths of the sequences, the zero-valued region of the kernel is extended with the same number of elements. The extension is distorted by the convolution, and discarding the padded region leaves the convolution undistorted and restores the length of the original sequence. The principle is illustrated in figure 3.1b. See [12, pp. 643-44] for a more in-depth treatment of the issue.

In the simulation, the number of zero-pads is determined by setting a tolerance for considering an element of the convolution kernel defined by $L(\Delta)$ to be non-zero and counting the number of non-zero elements. All sequences to be convolved are in total padded with the half number of non-zero elements. The kernel $L(\Delta)$ with half the number of pads in both beginning and end, and the Bloch components u, v and w as well as g with all the pads at the end, thus equal length of the sequences is maintained. Lastly, the Bloch components are cut off at the end, restoring the original length for use of the result as input for solving the Bloch equations in the nest time step. No cutting is needed for the kernel as a new kernel is defined in each time step. See lines 14 through 16 in appendix C for reference.

Before the simulation, a matrix for each of the Bloch components u, v and w, with dimension corresponding to the simulated time and detuning ranges, is initialised. The u and v matrices with all elements set to 0 and the w matrix with all elements set to -1 corresponds to the ensemble qubit being in a ground state $|g\rangle$. The use of the RK4 method is easily implemented as two nested loops; the outer loop stepping in time and the inner in detuning in this case. In each step of the outer loop, time step, the Bloch equations are solved by stepping in detuning (the inner loop) for the fixed time. The zero-padding and convolution described above is carried out at the end of the inner, detuning, loop. The result after the convolution is stored along the detuning dimension of the matrix and used as input for solving the Bloch equations in the next step of the outer, time, loop. The implementation of this procedure is found in program code 1 in appendix C.

Chapter 4

Results

The convolution as described in section 3.2 was introduced in the simulation and the efficiency for a pulse used experimentally for single qubit state transfers is presented in section 4.2. The scaling of the transfer fidelity with the size of the time step is of interest as the EFS model would not be valid unless the fidelity converges for smaller time step sizes. This is verified in section 4.3. Some numerical artefacts were observed which are mentioned in section 4.4. Some comments on the performance of the simulation conclude the chapter.

4.1 The Sechyp Pulse and Typical Population Curve Shape

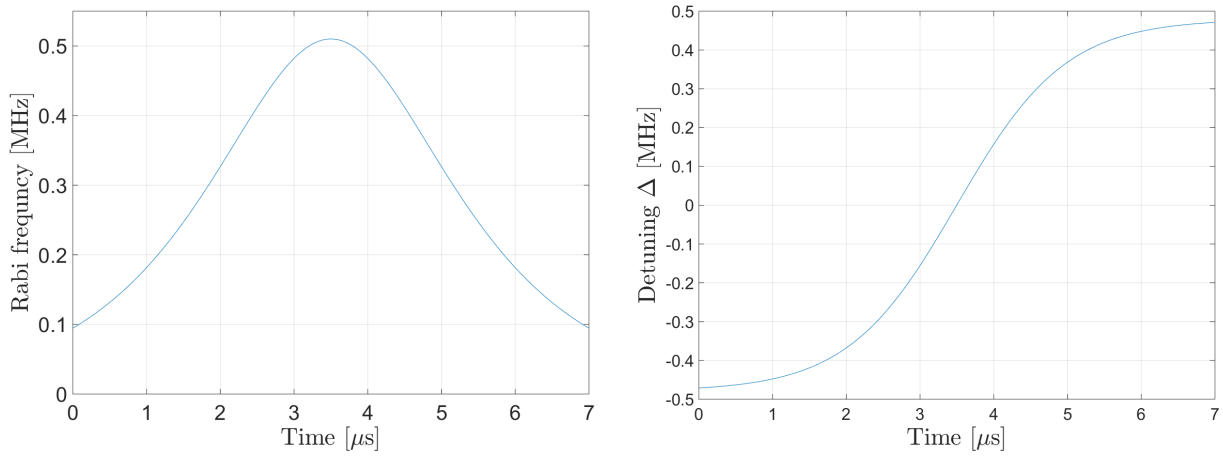

(a) **(b)**

Figure 4.1 The simulated pulse, with the same parameters as used in the single qubit transfer experiments in Eu:YSO. Pulse parameters are specified in table 4.1.

The pulse chosen for the simulation is one that was used in the preceding experiments carried out by the quantum information group. The pulse envelope, where the amplitude is 510 kHz, and corresponding sweep over the frequency domain are plotted in figure 4.1. Both plots show the full pulse duration of 7 µs. The parameters determining the pulse are presented in table 4.1. For reference, a typical population curve (without the

effects of EFS) resulting from the 7 µs pulse is provided in figure 4.2, and the width of the population curve agrees with the inversion stated in table 4.1 as well as the range of the sweep in figure 4.1b. In the results presented in the following sections, only the most relevant parts of the curve will be shown.

Parameter	**Value**
Pulse duration [µs]	7
Pulse centre [µs]	3.5
FWHM [µs]	2.6
Width of population inversion [kHz]	960
Rabi frequency Ω_0 [kHz]	510

Table 4.1 Parameters for the experimental pulse used in the simulation. The plots in figure 4.1 show the full duration of the pulse.

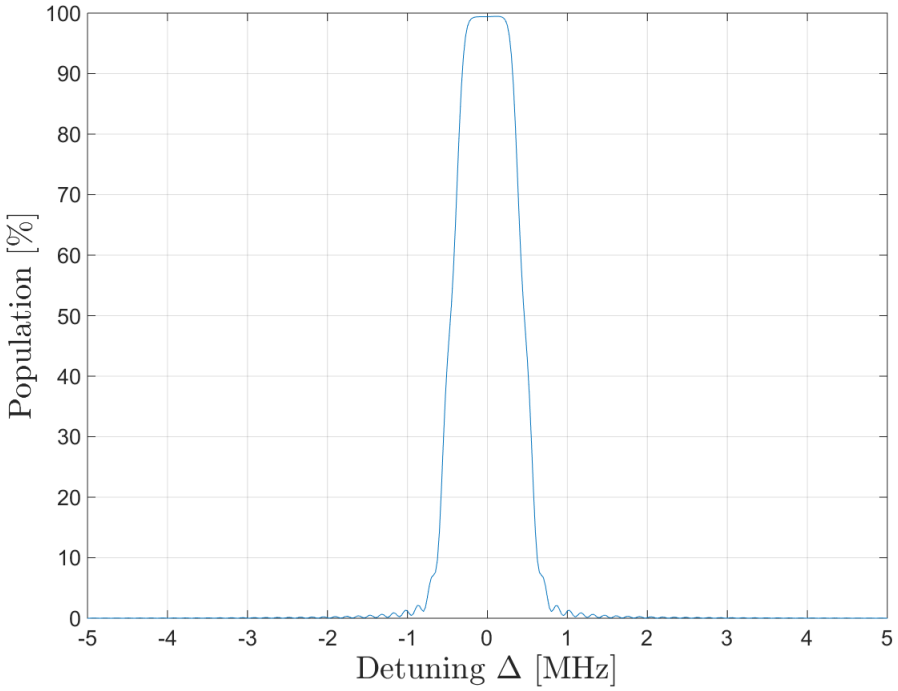

Figure 4.2 A typical population curve obtained for the pulse in figure 4.1.

4.2 Simulation of a Single Sechyp Pulse

The excited state population immediately after the pulse, with and without the impact of EFS, are plotted in figure 4.3. It shows the population in a range around its maximum, corresponding to the plateau of the curve in figure 4.2 outside which the population decreases rapidly. The upper curve corresponds to the RK4 solution the Bloch equations (2.4) only, and the lower to the solution including the effect of EFS, for the calculated interaction strength Γ_{efs} of 4.34 MHz. The input parameters for determining the convolution kernel $L(\Delta)$ and the strength of the dipole-dipole interaction Γ_{efs} are given in table 4.2.

Parameter	Value	Comment
Γ_{inh} [GHz]	2.5	For Eu^{3+} at site I [2, p. 117]
$\epsilon(0)$	7	[2, p. 129]
r_0 [nm]	0.24	[2, p. 133]
ζ_S [kHz/(V cm^{-1})]	35	[2, p. 117]
p	$1.25 \cdot 10^{-4}$	for 0.1% Eu^{3+} [2, p. 133]
$\langle\|\kappa\|\rangle$	0.7	see section 3.1 and [10]

Table 4.2 Parameters specific to the Eu:YSO crystal, used to determine the width of the convolution kernel Γ_{br}^{t} and the interaction strength Γ_{efs} in the simulation.

The upper curve in figure 4.3 has a maximum at 99.56% and the lower at 99.41%. This is to be compared to the experimental value of around 98% for the corresponding state transfer using the same pulse. However, the exact peak fidelities vary somewhat with the choice of time and detuning step sizes used in the simulation. The step sizes in the case presented here, given in table 4.3, are chosen to optimise the runtime while keeping the obtained fidelity in a range where it is roughly constant with changes in the time step size.

Fidelity	Value	Comment
RK4 solution (no EFS)	99.55%	4.7 ns time steps, 20 kHz detuning steps
With EFS	99.41%	$\Gamma_{efs} = 4.34$ MHz, step sizes as above
Experimental	98%	$\|g\rangle \rightarrow \|e\rangle$ transfer

Table 4.3 Comparison of fidelities obtained in simulation and experiment using the pulse described in section 4.1.

4.3 Fidelity Scaling With Time Step and Dipole Moment Magnitudes

A greater time step will result in a greater population difference from one time to the next in the integral (3.5) and thus a wider kernel with a greater smoothing effect from the EFS convolution, and vice versa. For the output of the simulation to be physical however, the absolute value of the population difference w has to converge towards some value smaller than or equal to 1, even though the smoothing effect decreases with the time step size. Assuming that the step size of the detuning grid is small enough to resolve the narrow convolution kernel $L(\Delta)$, the obtained fidelity is expected to vary very little with the time step size.

The fidelity was investigated for varying time step sizes, using the same sechyp pulse of duration 7 µs and amplitude $\Omega_0 = 510$ kHz, as specified in table 4.1. The maximum excited state population for a few different time step sizes are plotted in figure 4.4.

In order to further verify that the model behaves physically, the impact of varying difference in dipole moment between the ground and excited states was investigated. One would expect the EFS effects to be larger for increased $\delta\mu$ as the resulting changes in local electric field are increased, leading to larger frequency shifts. The difference in dipole moment $\delta\mu$ is proportional to the Stark coefficient ζ_S [2, p. 129], the value of ζ_S was varied in 5 kHz/(V cm^{-1}) increments, and the result is shown in figure 4.5.

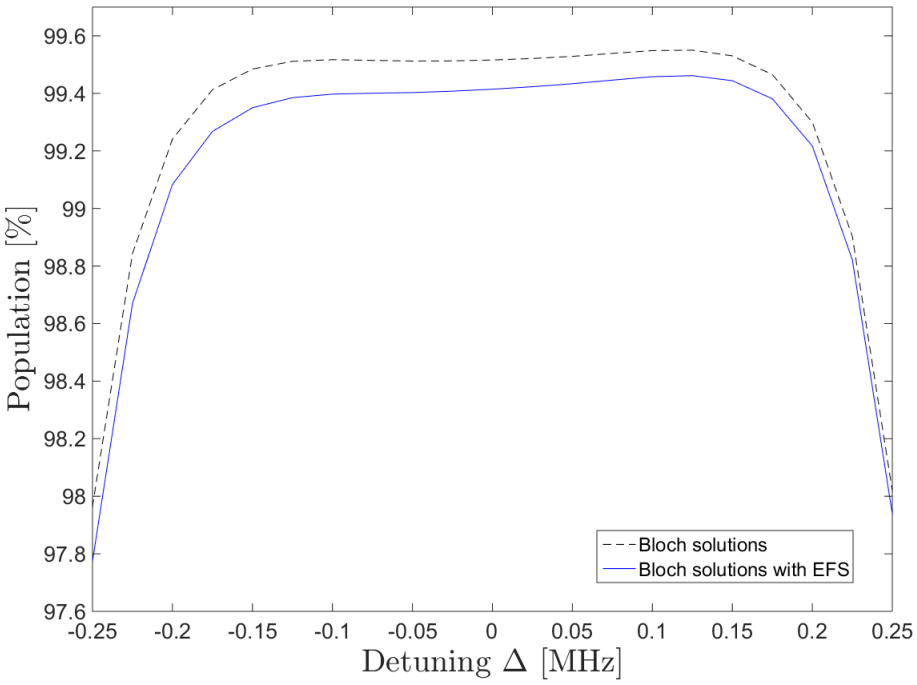

Figure 4.3 Simulated excited state population for a pulse of duration 7 µs and amplitude $\Omega_0 = 510$ kHz, specified by the parameters stated in table 4.1, with and without the effect of EFS. The upper curve has a maximum at 99.56% and the lower at 99.41%.

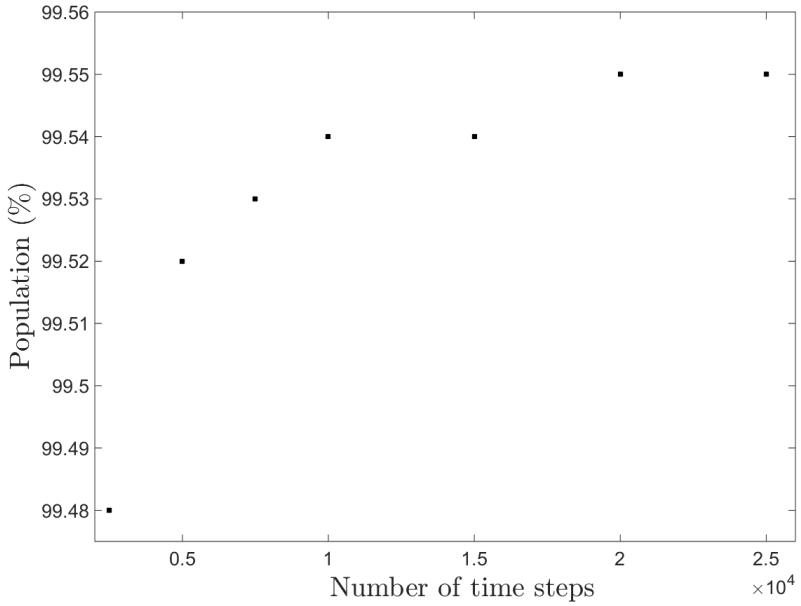

Figure 4.4 The maximum population obtained for the pulse in figure 4.1 in the presence of EFS when increasing the number of time steps, or equivalently decreasing time step size. Here the detuning step size is 25 kHz so the obtained maximum fidelity for 1500 time steps (approx. 4.7 ns steps) is not in agreement with the fidelity presented in section 4.2, where 20 kHz steps were used.

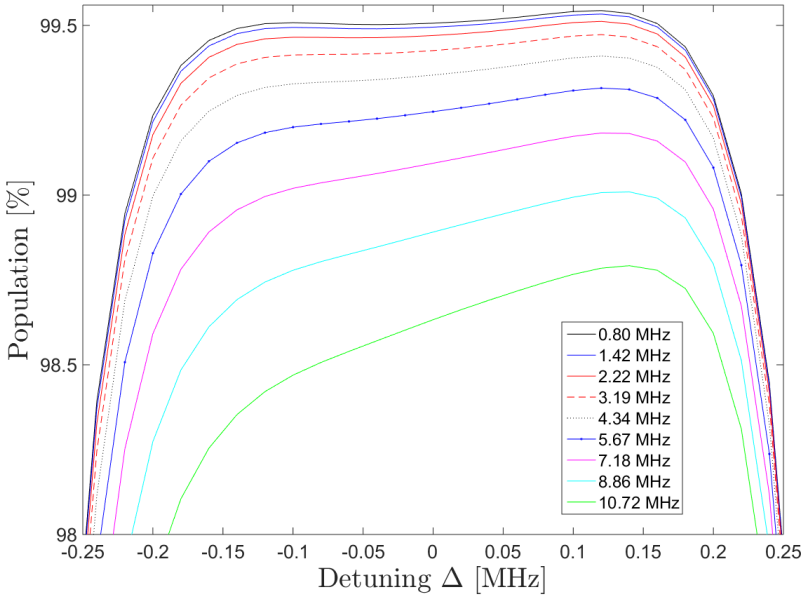

Figure 4.5 The centre of the population curve have been plotted for varying values of the Stark coefficient ζ_S is shown, corresponding to varying difference between the dipole moments of the ground and excited states. The legend displays the interaction strength Γ_{efs}, and the 4.34 MHz line is the same as the blue line in figure 4.3.

4.4 Possible Numerical Artefacts

A few potential numerical artefacts were noted during the work with the simulation. The first one to appear was leakage of the convolution kernel into the end-points of the simulation, as illustrated by figure 4.6, despite the zero-padding described in section 3.2. This effect is absent for the pulse considered above (see figure 4.2), however. Nevertheless, it could be of importance for other pulses one might want to investigate in the future.

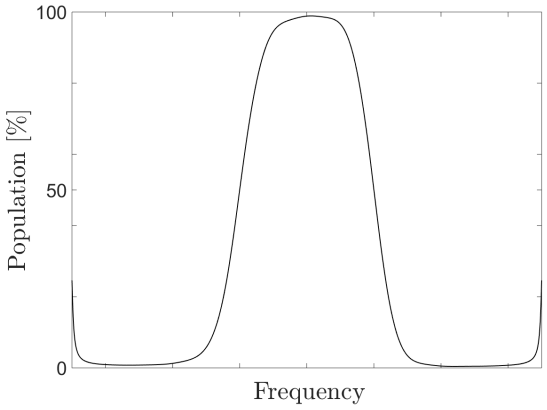

Figure 4.6 The population obtained for a pulse of higher amplitude, shorter duration and wider inversion than that considered in the text.

As visible in figure 4.2, the excited state population does not fall off smoothly to zero but oscillate slightly. A close-up of this pattern is shown in figure 4.7, the curves being from the same simulations as presented in section 4.2. Whereas the curves with and without EFS in figure 4.3 differ significantly around their maxima, they are seemingly equal around the end points of the population peak.

Furthermore, one can note that the population plateau is asymmetric and that the effect seem to increase with the interaction strength as apparent from figure 4.5. The effect is present although barely noticeable in the results without EFS, see the dashed curve in figure 4.3. Regardless of whether this effect is physical or a numerical artefact, it is amplified by the EFS convolution.

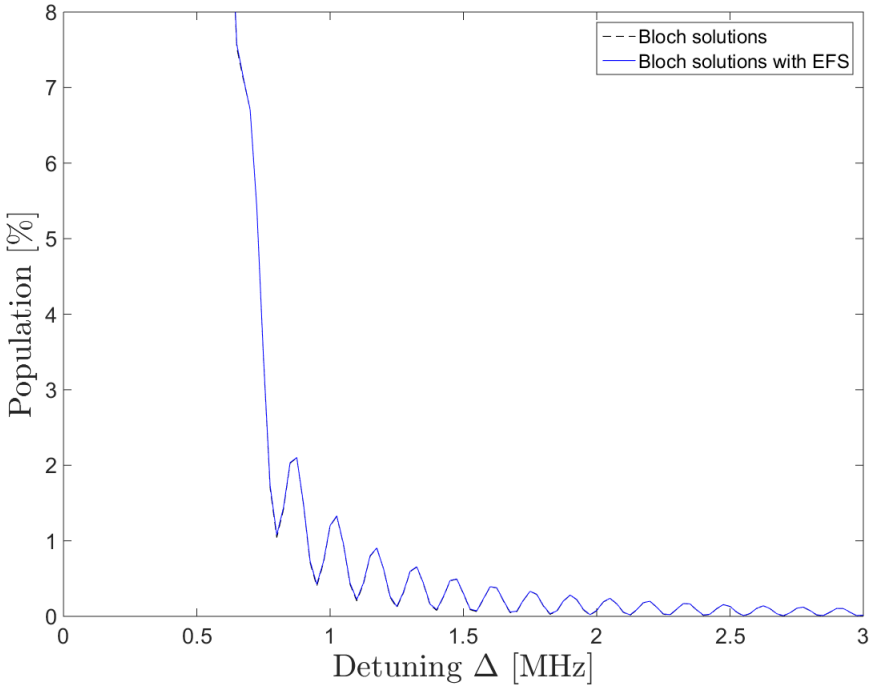

Figure 4.7 Oscillations was observed around one of the population end points. The same pattern can be observed towards the negative detuning end as well, see figure 4.2. Note that the result with and without EFS seem to be the same.

4.5 Comments Regarding Performance

The simulation was run on a 2.80 GHz Intel Core i7 CPU with 6 MB RAM. The simulation ran slowly at first before running out of memory for too small detuning steps (the time step size limit was never hit). The size and run time of the simulation have thus far been a limiting factor in investigating the model more thoroughly. As apparent from figure 4.4, the obtained excited state population are still increasing with the number of time steps. Of course, this limits the accuracy of the results from the simulation. The time and detuning step sizes used to obtain the results presented in this chapter are chosen somewhat arbitrarily, but such that sufficiently accurate results could be obtained in reasonable time.

Chapter 5

Conclusion

The comparison between the solution to the Bloch equations with and without the effects of the EFS in figure 4.3 shows only a small difference in population. This implies that the experimental loss of fidelity may not, for the most part, be due to EFS as described by the model discussed in section 3.1. The EFS convolution decreases the population transfer efficiency but too little to explain the experimental fidelity for the equivalent pulse, which is clear from comparing the experimental value of 98% with the loss from 99.55% without to 99.41% with EFS in the simulation. This is an interesting result, but there is reason to question some of the parameters used in and assumptions made or the simulation.

Chapter 6 of [2] compares experimental values of the Stark coefficient ζ_S. The text presents the result of 33.5 $\pm$ 1.5 kHz/(V cm^{-1}) whereas literature states 45.5 kHz/(V cm^{-1}). By inspecting the differences in population for varying ζ_S shown in figure 4.5, it becomes obvious that such a difference in ζ_S has a large impact on what fidelity in presence of EFS the simulation predicts. The value used was $\zeta_S = 35$ kHz/(V cm^{-1}), corresponding to the $\Gamma_{efs} = 4.34$ MHz graph in figure 4.5. The other graphs in the figure was obtained by varying ζ_S in increments of 5 kHz/(V cm^{-1}) and thus the 7.15 MHz graph corresponds to roughly the literature value stated in [2], predicting an excited state population slightly higher than 99%. Furthermore, the inaccuracy of the Eu concentration of the crystal used in the quantum information group's experiments is fairly large. If the dopant concentration happens to be higher than the 0.1% stated, thus increasing the dipole-dipole interaction, this in combination with the uncertainty in ζ_S could bring the fidelity predicted by the simulation much closer to the 98% found in the experiments, implying that EFS due to dipole-dipole interaction may very well be causing the low experimental fidelity.

There are of course other factors in how both the experiment and simulation were carried out that have an impact on the respective obtained fidelities. For an optimal pulse, the solution to the Bloch equations without EFS should predict the fidelity to be very close to 100%, only limited by relaxation during the pulse. As apparent from figure 4.3 however, this is not the case for the pulse considered here. Therefore, the appropriate value with which to compare the experimental fidelity is the 99.55% as predicted by the simulation without EFS. The effects relaxation could be minimised using pulse of higher Rabi frequency and shorter duration with the same pulse area, however requiring a more powerful laser set-up. Moreover, the experiment was designed to transfer a narrow ensemble of ions in their ground states, placed in an otherwise emptied spectral region, to the excited state. This structure was illustrated in figure 2.6. The actual shape of the ensemble in the ground state has not been taken into account by the simulation, where

ions within the range of the frequency sweep of the pulse are assumed to be distributed according to the inhomogeneous line shape $g(\Delta)$, without the preparation of a spectral pit. This distribution makes off-resonant excitations and interactions between the participating ions more probable. The effect of this should be a stronger decrease in the population obtained in the simulation with EFS included, thus making the EFS effects appear somewhat larger here than they would if a distribution of ions in the ground state more true to experiment had been assumed.

The asymmetrical shape of the populations in figure 4.3, amplified by the increased strength of the interaction considered in figure 4.5, have several possible physical explanations. A likely process that could explain why the population curve is lower towards negative detuning as is the case here, is that ions with resonance frequencies originally in the lower range are first excited, where the ones spatially close to an ion with higher resonance frequency could then be shifted towards higher frequencies as the pulse sweeps (see figure 4.1b). When the pulse sweeps through the even higher frequency range, the ions that were first excited could be in resonance once again and then driven back to the ground state, leaving the low-frequency population noticeably lower than for higher frequencies. This could also explain why the asymmetry is amplified with increased interaction strength; as it causes more ions to shift while in the excited state, more ions will be driven back as the pulse sweeps. Another explanation could be that the ions excited early relax during the sweep of the pulse, although the effect of this should be much smaller.

The oscillations seen in figure 4.7 is most likely a numerical artefact as there is nothing in the Bloch equations nor the EFS model suggesting this behaviour. Furthermore, the pulse, as plotted in figure 4.1a is cut off before reaching 0. This truncation is likely to cause the ringing pattern, which is a common error in algorithms based on FFT methods. As already mentioned in section 4.4, leaking of the kernel into the convolved population was not observed for the pulse considered in this text. However, running the simulation for a pulse of much higher intensity showed significant leakage as in figure 4.6. As this should have been corrected for by the zero-padding described in section 3.2, there is clearly a bug in the code performing the padding. For future use of the simulation, it is important to keep in mind that this bug may have a noticeable effect for other pulses. Also, this effect is largest in the end-points of the frequency range, so the wider the population inversion relative the simulated range is, the larger the impact on the population shape.

The result seem to converge toward some maximum fidelity for decreased size of the time step, as figure 4.4 shows. However, the obtained fidelity should also depend on the detuning step size but this dependence was not investigated. Decreasing the detuning step had a large impact on the runtime of the simulation, making such an investigation too time-consuming to be in scope of this thesis. It is nevertheless of great importance to know what the conditions are on the detuning step for the results of the simulation to be the foundation of more certain conclusions. A kernel much narrower than a detuning step could cause the smoothing effect to be too small, but as the increasing of the width of the kernel (see figure 4.5) seems to have a quadratic decrease of the maximum population as expected, it is likely that the detuning steps used are sufficiently small. The actual width of the kernel varies during the pulse however, why the smoothing effects may have been to small at the minimum widths for all widths considered. So although the relative scaling seems to be correct, it cannot be excluded that the magnitudes are shifted.

To summarise, it is an important piece of information that the effects of EFS seem to be small. To draw more certain conclusions however, the results need to be verified. Suggestions for further investigation and improvement is discussed in chapter 6.

Chapter 6

Outlook

It was concluded that broadening due to EFS as it is modelled here may not be the main cause of the lower-than-expected experimental fidelity results, but that further work is needed to verify the results presented in this thesis. Before other improvements however, fixing the most limiting bugs will be needed. First, the zero-padding bug mentioned in the section 4.4 would of course have to be fixed. As the work presented in this thesis is an extension to existing code, some design choices made in order to maintain compatibility has made it a little difficult to keep track of what secondary adjustments that may be needed when changing some parameter. This adds some degree of instability to the code, so it would be ideal to put some work into improving such issues as well.

To gain further insight in the fidelity losses through the model presented here, a more thorough understanding of the requirements on the time and detuning step sizes are for obtaining the correct simulation results is crucial. Too large step sizes will naturally be beyond the validity of the model, but smaller step sizes requires increasingly longer time for the simulation to run. Knowing the conditions for what sizes are small enough is necessary to determine what results are good enough and whether greater computational power is needed to obtain such results.

With the above mentioned bugs sorted out and the validity conditions for the simulation known, it could be interesting to investigate the fidelity of sequential state transfers. The transfer from ground to excited state considered here only constitutes part of a single qubit quantum gate. Several such transfers and transfers from the excited state to the other information-carrying ground state, is needed to construct a full quantum gate in the REQC scheme. Comparing the transfer-by-transfer loss of fidelity from simulation and from experiment could reveal further information about the performance of the scheme.

It possible that experimental work on single qubit transfers in Eu:YSO, as well as further analysis of existing data, could contribute to further understanding of the fidelity losses. One possibility is to investigate how the fidelity scales when varying the excitation density $\langle w \rangle$. This could verify whether the broadening effect Γ_{br} in equation (3.2) scales linearly with $\langle w \rangle$, or if there are additional processes contributing to the loss that need to be taken into account. Further, provided that the excitation density is related to the fidelity as the model predicts, one could try to verify the magnitude of Γ_{efs} by measuring Γ_{br} and $\langle w \rangle$ to get a hint whether the analytic expression (3.3) yields a similar magnitude.

In summary, the results found from this work suggest that the low fidelity, although at the time lower than needed for a working single qubit gate, does not necessarily mean the end for the REQC qubit. The results also provide hints for further work towards deeper insight into the physics and possible improvements of the implementation.

Appendix A

4th Order Runge-Kutta Solution to the Optical Bloch Equations

In the original code the optical Bloch equations were, for each Δ, solved with respect to t using the build-in MATLAB function `ode45`. Although this function is based on a Runge-Kutta method, it chooses its own time step size and prohibits the step-by-step access to the solution as required to model EFS as described in section 3.1. Also, as ions interact in the same way regardless of whether the excited ones were excited by a resonant or off-resonant frequency, the optical Bloch equations need to be solved for all detunings Δ in each time step. Therefore, the `ode45` function was replaced by a classical 4th order Runge-Kutta (RK4) method, as described in section 17.1 in [12] for example, but for solving three coupled equations of the form $\dot{y}_i = f_i(t, y_1, y_2, y_3, \Delta)$. The value of the i:th function y_i for the next time step $t + 1$ was given by

$$y(t+1, \Delta) = y(t, \Delta) + \frac{1}{6}\left[a_i + 2b_i + 2c_i + d_i\right], \tag{A.1}$$

where the coefficients a_i through d_i for a time step h are given by

$$\begin{aligned}
a_i &= h f_i\left(t, y_1, y_2, y_3, \Delta\right) \\
b_i &= h f_i\left(t + \frac{h}{2}, y_1 + \frac{1}{2}a_1, y_2 + \frac{1}{2}a_2, y_3 + \frac{1}{2}a_3, \Delta\right) \\
c_i &= h f_i\left(t + \frac{h}{2}, y_1 + \frac{1}{2}b_1, y_2 + \frac{1}{2}b_2, y_3 + \frac{1}{2}b_3, \Delta\right) \\
d_i &= h f_i\left(t + h, y_1 + c_1, y_2 + c_2, y_3 + c_3, \Delta\right).
\end{aligned} \tag{A.2}$$

The somewhat unconventional naming and indexing of the coefficients are chosen in order to be consistent with the variable names in the simulation code, where the roles of names and indices were swapped for ease of implementation.

Appendix B

Convolution Using Discrete Fourier Transforms

The convolution of a discrete signal s with some finite response function is mathematically defined as[12, p.642]

$$(s * r)_j = \sum_{k=-M/2+1}^{M/2} s_{j-k} r_k, \tag{B.1}$$

where M is the number of points in the response function. The discrete convolution theorem states that the discrete Fourier transform (DFT) of the convolution of a periodic function with a response function of finite duration [12, p. 642] correspond to the respective DFTs multiplied. This gives a way to compute convolutions fast, namely by taking the forward transforms of the functions, multiplying them, then taking the inverse transform to obtain the convolution[1]. The DFT X of a discrete sequence x of length N can be defined as

$$X(k) = \sum_{j=1}^{N} x(j) \exp(-2i\pi(k-1)(j-1)/N), \tag{B.2}$$

where the indices j and j have been shifted to account for MATLAB's one-based indexing of arrays. Conversely, the inverse counterpart becomes

$$x(j) = \frac{1}{N} \sum_{k=1}^{N} X(k) \exp(2i\pi(k-1)(j-1)/N). \tag{B.3}$$

[1] This is a result of applying the definition of the inverse DFT to the convolution theorem.

Appendix C

The Bloch Simulation Code

```
function [u,v,w] = Bloch_simulate(t,delta,u,v,w,T1,T2,...)
%[ see program code 2 ]
for time_count = 1:(length(t)-1)
    for delta_count = 1:length(delta)
        %[ see program code 3 ]
    end
    %Convolution with scrambing Lorentzian freq. shift
    dw = w(time_count+1,:)-w(time_count,:);
    integrand = 2*abs(dw).*g;
    gamma_br(time_count+1) = gamma_efs*trapz(delta,integrand);         %width of scrambler
    HWHM = gamma_br(time_count+1)/2;
    scrambler = HWHM./(pi.*((delta.^2)+(HWHM^2)));                     %smoothing kernel
    scrambler = scrambler./sum(scrambler);                             %normalisation for convolution
    tol = 0.0001e-5;        %padding with #elements larger than this
    response = scrambler(abs(scrambler) >= tol);
    K = ceil(length(response)/2);        %nbr of pads/2
    scrambler = padarray( scrambler, K , 'both' )';
    scrambler = ifftshift(scrambler);

    upad = padarray( u(time_count+1,:), 2*K , 'post')';
    vpad, wpad, gpad = ..."...;

    uconv = ifft( (fft( scrambler ) ).*( fft( upad ) ) );
    vconv, wconv, gconv = ..."...;

    u(time_count+1,:) = uconv(1:length(delta));
    v(time_count+1,:), w(time_count+1,:), g = ..."...;
    end
%[ see program code 4 ]
end
```

Program code 1 The smoothing of the Bloch equation solutions at the end of the time loop.

```
%Physical constants
    gamma_inh           = 2.5e9*2*pi;     %Hz inhomogeneous linewidth Graf p. 117
    epsilon_vac         = 8.854e-12;      %As/Vm
    epsilon_0           = 7;              %As/Vm Graf p. 129
    r0                  = 2.4e-10;        %m, Graf p. 133
    planck              = 6.626e-34;      %Js
    zeta                = 35e1;           %Hz/(Vm-1), Graf p. 117
    occ_prob            = 1.25e-4;        %at 0.1% Eu3+ (Graf p 133)
    ave_kappa           = 0.7;
    D0                  =                                                   ...
     ↪  planck*(zeta^2)/(2*epsilon_0*epsilon_vac*(r0^3));
    gamma_efs           = pi*occ_prob*D0*(1/3)*ave_kappa;   %Hz


    %Definition of a half-step time for evaluating the Rabi frequency
    tstep = t(2) - t(1);
    t_half = (t(1):tstep/2:t(end));
                            %vector of same range as t in steps of tstep/2, odd-incided elements equal to t
    whole_ind = (1:2:length(t_half));
                            %odd-indices mapping to elements in t_half corresponding to points in t
    half_ind = (2:2:length(t_half));
                            %even-indices mapping to elements in t_half corresponding to intermediate midpoints of t

    %Evaluating the Rabi frequency at in half steps for usen in RK4
    f = fcnchk(pulse{1});
    OmegaRcomplex = f(t_half, pulse{2:end});
    OmegaRre      = real(OmegaRcomplex);
    OmegaRim      = imag(OmegaRcomplex);

    %Initialising inh profile for EFS convolution
    g = gamma_inh./(2*pi*(delta.^2+(gamma_inh/2)^2));                       ...
     ↪  %original inhomogeneous profile, function of delta
    g = g./trapz(delta,g);
    gamma_br = zeros(size(t(1:end-1)));
```

Program code 2 Definition of physical constants and initialisation of the vectors `OmegaRre`, `OmegaRim` and `g`. `g` is normalised such that it's integral over the detuning range is equal to 1.

```
function [u,v,w] = Bloch_simulate(t,delta,u,v,w,T1,T2,...)
%[ see program code 2 ]
for time_count = 1:(length(t)-1)
    whole_count = whole_ind(time_count);
    half_count = half_ind(time_count);

    for delta_count = 1:length(delta)
        current_delta = delta(delta_count);

        %RK4 soln to Bloch eqns
        A = tstep*bloch_eq([u(time_count,delta_count),                ...
        ↪  v(time_count,delta_count),                                 ...
        ↪           w(time_count,delta_count)], ...
            T1,T2,current_delta,OmegaRre(whole_count),                ...
            ↪  OmegaRim(whole_count));

        B = tstep*bloch_eq([u(time_count,delta_count)+(1/2)*A(1),     ...
        ↪  v(time_count,delta_count)+(1/2)*A(2), ...
            w(time_count,delta_count) + (1/2)*A(3)],                  ...
            ↪  T1,T2,current_delta,OmegaRre(half_count),              ...
            ↪  OmegaRim(half_count));

        C = tstep*bloch_eq([u(time_count,delta_count)+(1/2)*B(1),     ...
        ↪  v(time_count,delta_count)+(1/2)*B(2), ...
            w(time_count,delta_count) + (1/2)*B(3)],                  ...
            ↪  T1,T2,current_delta,OmegaRre(half_count),              ...
            ↪  OmegaRim(half_count));

        D = tstep*bloch_eq([u(time_count,delta_count)+C(1),           ...
        ↪  v(time_count,delta_count)+C(2), ...
        w(time_count,delta_count) + C(3)],                            ...
        ↪  T1,T2,current_delta,OmegaRre(whole_count+1),               ...
        ↪  OmegaRim(whole_count+1));

        u(time_count+1, delta_count) = u(time_count, delta_count) +   ...
        ↪  (1/6)*(A(1) + 2*B(1) + 2*C(1) + D(1));
        v(time_count+1, delta_count) = v(time_count, delta_count) +   ...
        ↪  (1/6)*(A(2) + 2*B(2) + 2*C(2) + D(2));
        w(time_count+1, delta_count) = w(time_count, delta_count) +   ...
        ↪  (1/6)*(A(3) + 2*B(3) + 2*C(3) + D(3));
    end
%[ see program code 1 ]
end
```

Program code 3 The RK4 solution to the Bloch equations of the form (A.1) with coefficients as in equation (A.2). The function `bloch_eq` (see program code 4) returns three vectors containing the respective evaluations of the Bloch equations (2.4) for the passed input arguments. For definition of the pulse variables `OmegaRre` and `OmegaRim`, see program code 2

```
function dy = bloch_eq(y,T1,T2,Delta,OmegaRre, OmegaRim)
dy = zeros(3,1);
dy(1) = -1/T2*y(1)-Delta*y(2)+OmegaRim*y(3);
dy(2) = Delta*y(1)-1/T2*y(2)+OmegaRre*y(3);
dy(3) = -OmegaRim*y(1)-OmegaRre*y(2)-1/T1*(1+y(3));
end
```

Program code 4 The function returning the evaluation of the Bloch equations, as defined in equation (2.4), called when calculating the RK4 coefficients (A.2) in program code 3.

Bibliography

[1] M. A. Nielsen and I. L. Chuang, *Quantum Computation and Quantum Information: 10th Anniversary Edition* (Cambridge University Press, 2011), ISBN 1107002176.

[2] F. R. Graf, *Investigations of spectral dynamics in rare earth ion doped crystals using high resolution laser techniques (Diss. ETH No 12623)* (Swiss Federal Institute of Technology, 1998).

[3] G. W. Burr, T. L. Harris, W. R. Babbitt, and C. M. Jefferson, Journal of Luminescence **107**, 314 (2004).

[4] D. P. DiVincenzo, Tech. Rep., IBM (2008), 0002077v3.

[5] M. Nilsson, *Coherent Interactions in Rare-Earth-Ion-Doped Crystals for Applications in Quantum Information Science* (Lund Institute of Technology, 2005), ISBN 91-628-6377-0.

[6] L. Rippe, *Quantum computing with naturally trapped sub-nanometre-spaced ions* (Lund Institute of Technology, 2006), ISBN 978-91-628-6907-6.

[7] C. Foot, *Atomic Physics* (Oxford University Press, 2005), ISBN 978 0 19 850696 6.

[8] J. H. Wesenberg and K. Mø lmer, Physical Review Letters **93**, 143903 (2004), 0406178.

[9] Y. Yan, J. Karlsson, L. Rippe, A. Walther, D. Serrano, M.-E. Pistol, S. Kröll, P. Goldner, L. Zheng, and J. Xu, Physical Review B - Condensed Matter and Materials Physics **87**, 184205 (2013).

[10] S. B. Altner, G. Zumofen, and U. P. Wild, Physical Review B **54**, 17493 (1996).

[11] G. Mahan, Physical Review **153**, 983 (1967).

[12] W. H. Press, S. A. Teukolsky, W. T. Vetterling, and B. P. Flannery, *Numerical Recipes: The Art of Scientific Computing* (Cambridge University Press, 2007), 3rd ed., ISBN 0521880688.